Journal of Sol-Gel Science and Technology (2019) 92:415–426
https://doi.org/10.1007/s10971-019-04979-4

ORIGINAL PAPER: FUNCTIONAL COATINGS, THIN FILMS AND MEMBRANES (INCLUDING DEPOSITION TECHNIQUES)

Check for updates

Gas-sensing properties of nanostructured TiO_2–$xZrO_2$ thin films obtained by the sol–gel method

Artem S. Mokrushin[1] · Elizaveta P. Simonenko[1] · Nikolay P. Simonenko[1] · Kirill A. Bukunov[2,3] · Philipp Yu. Gorobtsov[1] · Vladimir G. Sevastyanov[1] · Nikolay T. Kuznetsov[1]

Received: 20 December 2018 / Accepted: 21 March 2019 / Published online: 30 March 2019

Abstract

TiO_2–$xZrO_2$ films of various phase compositions were synthesized by sol–gel technique. According to the Raman spectroscopy, data films with $x = 0$–20% possess an anatase crystal structure, with $x = 40\%$, exhibiting zirconium titanate $ZrTiO_4$ structure and a film with $x = 50\%$ is amorphous. Anatase-structured films demonstrate a high and reproducible response to oxygen in a wide range of concentrations (1–20%) under temperatures of 400–450 °C. The film with 10% ZrO_2 exhibits the best response, which is in particular attributed to the lower particle size of the coating compared with that of other films. It was shown that the response to oxygen upon increasing the operating temperature from 400 to 450 °C diminishes much less in the case of titanium dioxide doped with 10% ZrO_2, than in the case of pure TiO_2. Introduction of the Zr^{4+} ion into the anatase crystal structure also decreases the baseline drift. It was shown that thin films of TiO_2–$xZrO_2$ (with $x = 0$ and 10%), obtained in this study, possess a good selectivity to oxygen; the response to other analyte gases (H_2, CH_4, and CO) does not exceed 1.6 and 1.4 under the temperatures of 400 and 450 °C, respectively.

Graphical Abstract

TiO_2–$xZrO_2$ films of various phase composition were synthesized by sol–gel technique. According to the Raman spectroscopy data films with $x = 0$–20% possess an anatase crystal structure, with $x = 40\%$ exhibit zirconium titanate structure and film with $x = 50\%$ is amorphous. Anatase-structured films demonstrate high and reproducible response to oxygen in the wide range of concentrations (1–20%) under temperatures of 400–450 °C.

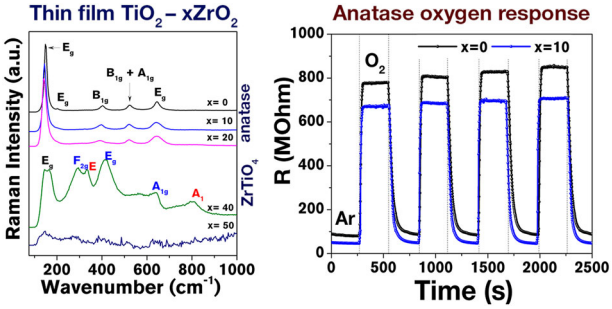

Supplementary information The online version of this article (https://doi.org/10.1007/s10971-019-04979-4) contains supplementary material, which is available to authorized users.

✉ Artem S. Mokrushin
artyom.nano@gmail.com

[1] Kurnakov Institute of General and Inorganic Chemistry of the Russian Academy of Sciences, 31 Leninsky pr., Moscow 119991, Russia

[2] Faculty of Physics Lomonosov Moscow State University, 1-2 Leninskie Gory, 119991 Moscow, Russia

[3] Skobeltsyn Institute of Nuclear Physics Lomonosov Moscow State University, 1-2 Leninskie Gory, 119991 Moscow, Russia

Highlights

- TiO_2–$xZrO_2$ films and powders were synthesized by sol–gel technique.
- TiO_2–$xZrO_2$ ($x = 0$–20 mol.%) possess anatase structure.
- A film with $x = 40\%$ has zirconium titanate structure, a film with $x = 50\%$ is amorphous.
- Anatase-structured films exhibit a high reproducible response to O_2.
- The film with $x = 10\%$ possesses the best response to O_2.

Keywords Sol–gel · TiO_2 · Zirconium titanate · Gas sensor · Thin films · Raman spectroscopy

1 Introduction

In the last two decades, titanium dioxide became one of the most popular and widely used functional materials. The whole spectrum of unique electrophysical and chemical characteristics possessed by TiO_2, its n-type semiconductor properties, capacity to luminescent oxygen non-stoichiometry, biological compatibility, and low toxicity allow to utilize it in a wide range of science and technology applications [1]. There is an enormous number of sublime articles concerning different applications of titanium dioxide. It is used both in everyday life and in scientific tasks, examples of the former being the use as a component of pigments, paint, sunscreen materials, salves, and toothpaste, and examples of the latter applications include photovoltaics, photocatalysis, solar energy devices, chemical gas sensors, as an electrode material in lithium-ion batteries, and as a component of biomedical implants [2–6].

Titanium dioxide, as well as tin dioxide [7–9] and zinc oxide [10, 11], is one of the most popular receptor material in chemical gas sensors [12]. N-type semiconductor properties (band gap is ~3.2 eV [13, 14] for anatase crystal structure) allow titanium dioxide and its nanocomposites to exhibit a resistive response to a wide range of analyte gases, such as H_2 [15–17], NO_2 [18], CO [18], NH_3 [18], volatile organic compounds (VOC) [19–21], and other analytes [20, 22], while the capacity to luminescence allows to generate additional charge carriers and thus to lower the operating temperature and increase the response [23–25]. Oxygen non-stoichiometry and the presence of oxygen vacancies, as in the case of CeO_2 [26–28], make titania the most convenient receptor material for resistive detection of oxygen [29–35]. There are many studies concerning the effect of various dopants, such as ZnO [35], CeO_2 [29, 36], V_2O_5 [37], and others [31, 38], on the signal obtained while sensing oxygen with titanium dioxide. In our opinion, TiO_2–ZrO_2 binary system is very interesting for oxygen detection. Both zirconia and titania have oxygen vacancies in their crystal structures, and so the former may also be utilized for resistive sensing of oxygen [39], but under considerably higher operating temperatures. Nanomaterials based on TiO_2–ZrO_2 compounds, as well as individual titanium dioxide, are indeed utilized as receptor materials for detecting analyte gases [40–42] in sensors of various types. But papers on using TiO_2–ZrO_2 nanomaterials as a responsive layer in chemiresistive gas sensors are almost nonexistent, except for a study by Mohammadi et al. [40], in which a thin two-phase TiO_2–ZrO_2 film was obtained by sol–gel technique for sensing 0.5–200-ppm CO under the operating temperature of 150 °C.

Doping TiO_2 with ZrO_2 can result in solid solution with anatase or rutile structure, depending on the heat treatment, and can also give rise to zirconium titanate $TiZrO_4$ [43–48], which unlike titania and its solid solutions, is a dielectric and is used as a resonator component [49–51], and also as a humidity sensor [52, 53] under high temperatures of > 600 °C.

Synthesis of titania thin films for chemical gas sensors is carried out by utilizing both liquid-phase approaches (such as sol–gel [54], solvothermal, and hydrothermal [1]) and gas-phase approaches (CVD and PVD [55, 56], magnetron-sputtering deposition [57], and atomic layer deposition (ALD) [58]).

Sol–gel technique is very convenient for obtaining thin oxide coatings, and it is of complex composition in particular. Precursor solutions in such approaches are mostly deposited utilizing traditional techniques such as dip- and spin-coating, but the high-resolution ink-jet printing is considered a very promising approach [59].

The goal of this work was to synthesize thin nanostructured TiO_2–$xZrO_2$ ($x = 0$, 10, 20, 40, and 50 mol.%) films utilizing sol–gel technique, study of their phase composition, microstructure, and chemiresistive gas-sensing properties, especially oxygen detection.

2 Experimental

Preparation of zirconium acetylacetonate $[Zr(O_2C_5H_7)_4]$ was carried out using $ZrOCl_2 \cdot 8H_2O$ (cp) and acetylacetone $C_5H_8O_2$ (pure) upon their solution neutralization with 5% aquatic solution of $NH_3 \cdot H_2O$ (hp); thus, the obtained compound was dried at 50 °C until its mass stabilized. The resulting product was identified using IR spectroscopy, powder XRD, and simultaneous DTA/DSC/TGA. Titanium tetrabutoxide (pure) was also utilized in synthesis.

Electron (UV-) spectra of precursor solutions were recorded after their dilution with propanol (>99%) to 4×10^{-4} mol/l concentration (cell thickness was 1 mm) with UV-Vis spectrometer SF-56.

IR transmittance spectra of heteroligand complex solutions were recorded with InfraLUM FT-08 IR-Fourier spectrometer.

The changes in the rheological properties of the heteroligand precursor solutions were studied utilizing Fungilab Smart L rotational viscosimeter; the shear rate was 100 RPM, the spindle used was L2.

Thermal behavior of the xerogel was analyzed with use of a synchronous DSC/DTA/TG analyzer SDT-Q600 (TA Instruments) in Al_2O_3 crucibles in air flow (ml/min), the heating rate was 10 °C/min.

X-ray diffraction patterns of oxide powders and film surfaces were obtained using D8 Advance (Bruker) X-ray diffractometer in the range of 2θ 5–80° with a resolution of 0.02°, signal accumulation time for each point was 0.3 s, except for 2θ 27–33°, where accumulation time was 2.0 s.

Raman spectra were registered with NT-MDT INTEGRA Spectra device, the laser wavelength was 473 nm. For powders, the lens used was 100 × 0.28 NA, pinhole: 50 µm, monochromator grating was 1800/500 [mm^{-1}/nm], intensity in the sample was ~8 mW, and diameter of a focused laser beam on the sample surface was ~30–50 µm. For thin films, the lens used was 100 × 0.9 NA, pinhole: 100 µm, monochromator grating was 1800/500 [mm^{-1}/nm], intensity on the sample was ~8 mW, and diameter of the focused laser beam on the sample surface was ~3 µm.

Powder morphology was investigated using NVision 40 (Carl Zeiss) workstation. Film microstructure was investigated utilizing high resolution SEM Supra 50 VP LEO (Carl Zeiss) and SPM Solver Pro-M (NT-MDT); the latter was performed in semi-contact mode with NT-MDT NSG-10 probes.

Gas-sensing properties were measured on a special precision setup. Gas environment was generated in a quartz cell with the use of two Bronkhorst gas flow controllers with maximal flow of 100 and 200 ml/min. Gas flow thus achieved had a stability of ± 0.5 ml/min. Sensor element temperature was regulated utilizing a platinum microheater. The sensitivity of the synthesized 2D nanomaterials to analyte gases O_2, H_2, CH_4, and CO was investigated. In the case of oxygen detection, the baseline was recorded in the argon environment, while in other cases, synthetic air was used. Oxide film resistance was measured on the Fluke 8846 A (6.5 Digit Precision Multimeter) digital multimeter with the upper limit of 1 GΩ. Operating temperature did not exceed 450 °C (which is 50 °C less than the oxide crystallization temperature), in order to prevent changes in dispersity and microstructure that could result from aggregation of nanomaterial particles.

Oxygen response was calculated with this formula:

$$S_1 = R_{O2}/R_{Ar} \quad (1)$$

with R_{O2} being the resistance of a given oxide film in the environment with set O_2 concentration; R_{Ar} being the resistance of the same oxide film in argon atmosphere.

Responses to H_2, CH_4, and CO were calculated according to the formula:

$$S_2 = R_{air}/R_{gas} \quad (2)$$

with R_{air} being the resistance of a given oxide film in air and R_{gas} being the resistance of the same oxide film in gas–air mixture with a set analyte gas concentration.

3 Results and discussion

3.1 Preparation of hydrolytically active heteroligand precursors

The isoamyl alcohol solution of the earlier obtained [$Zr(O_2C_5H_7)_4$] complex was subjected to thermal treatment at the temperature of ~131 °C for 30 min in a round-bottom flask with a reflux. During this process, the destructive substitution of chelate $O_2C_5H_7$ ligand for alkoxo fragments occurred [39, 60, 61]. The degree of ligand substitution was determined from the decrease in the intensity of the absorption band at 250–340 nm, which is characteristic of the acetylacetonate group, on the electron (UV-) spectra of solutions before and after thermal treatment. For the prepared [$Zr(O_2C_5H_7)_{4-x}(OC_5H_{11})_x$], the solution degree of $O_2C_5H_7$-ligand substitution was 84%. IR-spectroscopy data also confirmed the occurrence of a partial destructive substitution of $O_2C_5H_7$-ligands, which gave yield to acetone and isoamylacetate. It was inferred from the simultaneous decrease in the intensity of the absorption bands with peaks at 1540 and 1590 cm^{-1}, which are characteristic of C=C and C=O bonds in coordinated chelate groups, and emergence of a characteristic double-absorption band with peaks in the region of 1700–1750 cm^{-1} (Fig. S1).

Afterward, tetrabutoxititanium was added to thus-obtained zirconium-including solution in required quantities (derived from the stoichiometry of a target complex TiO_2–$xZrO_2$ oxide). The overall metal concentration was brought to 0.2 mol/l by the addition of isoamyl alcohol. The dynamic viscosity of thus-prepared solutions was measured on Brookfield rotational viscometer and was about 7 cP.

3.2 Preparation of thin nanostructured TiO_2–$xZrO_2$ films

Thin films of precursor solutions were deposited onto the surface of polycrystalline Al_2O_3 substrates with counter-pin

platinum electrodes and a microheater, utilizing the dip-coating technique with a rate of retrieval of 1 mm/s [39, 54, 58, 61–63]. The air moisture then initiated processes of hydrolysis and self-assembly by polycondensation in the volume of the films. Afterward, the samples were dried step by step in the range of 22–50 °C, which resulted in the conclusion of gel syneresis and formation of xerogel coatings.

Aliquots were taken from precursor solutions to investigate the process of TiO_2–$xZrO_2$ ($x = 0$, 10, 20, 40, and 50 mol.%) nanopowder preparation. Hydrolysis of samples in this case was also performed by the air moisture after solvent removal. From the analysis of TGA-DSC data for powders (Fig. S2), the optimal conditions for anatase phase crystallization were determined, which turned out to be heat treatment at 500 °C for 1 h. These conditions were then used to obtain both thin oxide films and powders of TiO_2–$xZrO_2$ composition.

XRD patterns for TiO_2–$xZrO_2$ ($x = 0$, 10, 20, 40, and 50 mol.%) powders are presented in Fig. 1. From the characteristic reflex patterns, we can infer that the powders with 0–20% ZrO_2 have anatase crystal structure [64, 65], while the last compound ($x = 50\%$) is amorphous. Mean crystallite size calculated from complete peak profile analysis is 24 nm for TiO_2, while for the composition with 10 mol.% ZrO_2, this number increases to 72 nm. For the last two compositions of TiO_2–$xZrO_2$ ($x = 40$ and 50 mol.%) powders are X-ray amorphous. In the case of thin films, X-ray diffraction patterns are rather scarce on information, due to the fact that the most intensive reflex of anatase at (101) is completely covered by background from the α-Al_2O_3 substrate [66].

Raman spectra for powders are presented in Fig. 2a and those for films are featured in Fig. 2b. It is seen from these

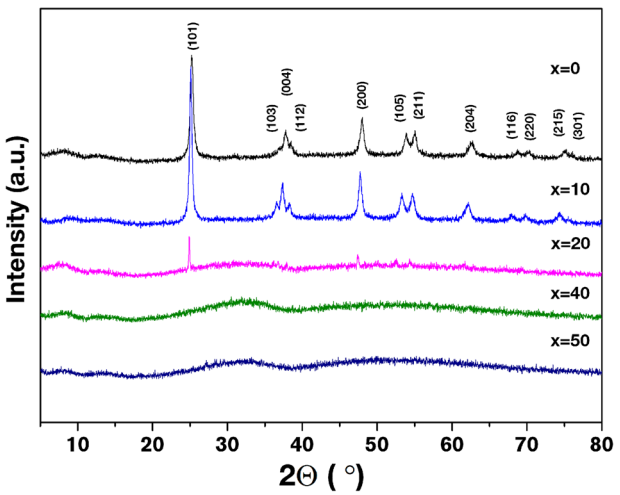

Fig. 1 XRD patterns for TiO_2–$xZrO_2$ powders ($x = 0$, 10, 20, 40, and 50 mol.%)

spectra that both for powders and films of TiO_2–$xZrO_2$ ($x =$ 0, 10, and 20 mol.%), compositions of four modes are observed with maximum values at 145 (E_g), 638 (E_g), 397 (B_{1g}), and 518 cm^{-1} (A_{1g} or B_{1g}), which are characteristic of anatase crystal structure [67, 68], while for powders and films of pure TiO_2 and including 10 mol.% ZrO_2, an additional low-intensity E_g band is observed at 155 cm^{-1}, which is also characteristic of anatase. Upon the increase of ZrO_2 content to 20%, the E_g mode at 155 cm^{-1} widens and further decreases in intensity. Powders of TiO_2–$xZrO_2$ ($x = 40$ and 50 mol.%) do not exhibit modes, characteristic for crystalline TiO_2, ZrO_2, and $ZrTiO_4$, and are amorphous, which correlates with XRD data.

In contrast to the powder, the thin film of TiO_2–$xZrO_2$ ($x = 40$ mol.%) exhibits six vibrational modes at 157 (E_g), 296 (F_{2g}), 331 (E), 416 (E_g), 640 (A_{1g}), and 802 cm^{-1}(A_1), which are characteristic for $TiZrO_4$ crystal structure [69, 70]. A film of TiO_2–$xZrO_2$ ($x = 50$ mol.%) composition, as well as a powder of the same composition, has no characteristic bands and stays amorphous at the chosen treatment conditions for xerogels.

Both the powders and the thin films of the Raman spectra exhibit a broadening and a shift of the main mode, corresponding to the anatase structure (E_g) to the lower wave number region with an increase in the ZrO_2 content from 10 to 20%. A number of factors could contribute to such changes, namely nanomaterial dispersity, thermal effect on the grains, which depends on the laser power during measurements, nanomaterial nature and dispersity, the phonon confinement, and change in the lattice parameters, e.g., due to formation of solid solutions. Determining the degree of influence for any one of the enumerated factors represents an extraordinary task, both theoretically and experimentally. It was shown in a study [71] that the increase of lattice parameters is the main contributor to the E_g mode shift in the TiO_2–ZrO_2 system (due to the fact that the zirconium cation radius is much larger than that of titanium ($r(Zr^{4+}) =$ 0.84 Å, $r(Ti^{4+}) = 0.60$ Å [72]). Authors of ref. [71] demonstrated that the E_g mode shift perfectly correlates with changes in its full width at half maximum, FWHM, which increases at ZrO_2 content > 8%. In our case, it is obvious that dispersity does not affect broadening shifting of the mode, since with doping anatase structure with Zr^{4+}, mean particle size increases in powders and decreases in films. Thus, we can state that the shift and broadening of the E_g mode at 144–141 cm^{-1} for TiO_2–$xZrO_2$ ($x = 10$ and 20 mol.%) compared with its parameters for individual TiO_2 (149–151 cm^{-1}) is first of all associated with formation of solid solution based on anatase phase with the corresponding increases in lattice parameters.

The microstructure of the obtained TiO_2–ZrO_2 powders was studied with a scanning electron microscope (SEM). On the featured microphotographs (Fig. 3a, b), it is seen that for

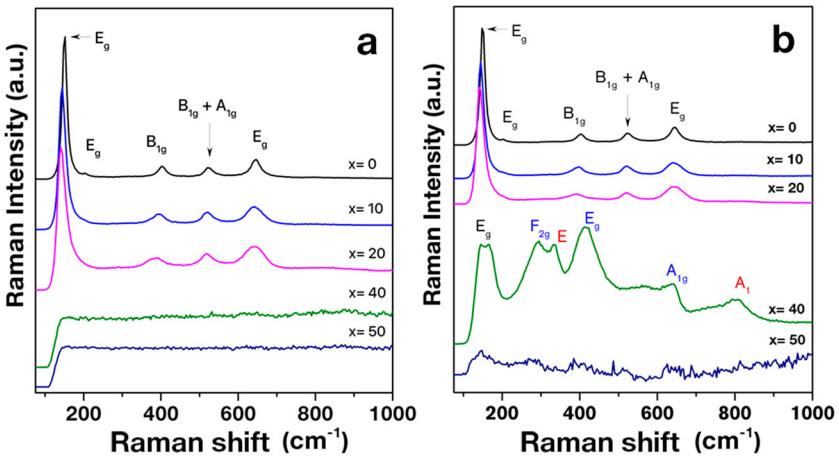

Fig. 2 Raman spectra for powders **a** and films **b** for TiO_2–$xZrO_2$ ($x = 0$, 10, 20, 40, and 50 mol.%) compositions

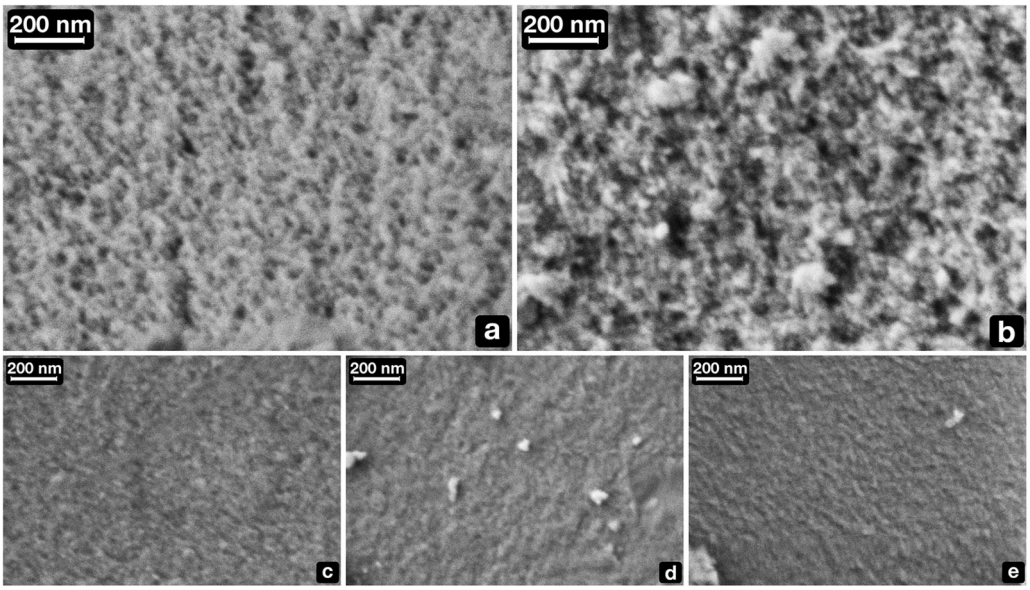

Fig. 3 SEM microphotographs for TiO_2–$xZrO_2$ ($x = 0$ **a**, 10 **b**, 20 **c**, 40 **d**, and 50 **e** mol.%) powders

powders with anatase crystal structure, a porous morphology with a mean particle size of 33 ± 5 nm (for pure TiO_2) and 62 ± 5 nm (composition with 10 mol.% ZrO_2) is observed. Powders of TiO_2–$xZrO_2$ ($x = 20$, 40, and 50 mol.%) compositions, which are completely or partially amorphous according to the XRD and Raman spectroscopy data, have a dense microstructure (Fig. 3c–e) with a mean particle size of 36 ± 5, 41 ± 6, and 30 ± 4 nm accordingly.

Morphology of the prepared thin TiO_2–$xZrO_2$ films is presented in Fig. 4. In contrast to powders, thin films are more highly disperse. A pure TiO_2 film (Fig. 4a) has a mean particle size of 13 ± 2 nm, while on addition of 10% ZrO_2 (Fig. 4b), a drop to 9 ± 1 nm in the mean particle size is observed. A film of TiO_2–$xZrO_2$ ($x = 20$ mol.%) composition is composed of particles (Fig. 4c) with a mean particle size of 28 ± 7 nm.

Despite the powder of TiO_2–$xZrO_2$ ($x = 40$ mol.%) composition being amorphous (Figs. 1, 2a), the corresponding film crystallized with formation of srilankite $TiZrO_4$ structure (possibly, phase nanodomains started to form at these conditions). The microstructure is presented in Fig. 4d; the mean particle size observed is 9 ± 2 nm. Such unorthodox behavior (in thin-film crystallization is usually observed at higher temperatures than in powders) can be attributed to the effect of the α-Al_2O_3 substrate. It is seen from the literature data (Table 1) that lattice parameters *a* and *b* for srilankite are quite close to the parameters for the α-Al_2O_3 substrate, which was used for film deposition. It is due to this that the $TiZrO_4$ crystal phase formation occurred specifically in the thin film on the α-Al_2O_3 (which can be observed from the Raman spectroscopy data present in Fig. 2b).

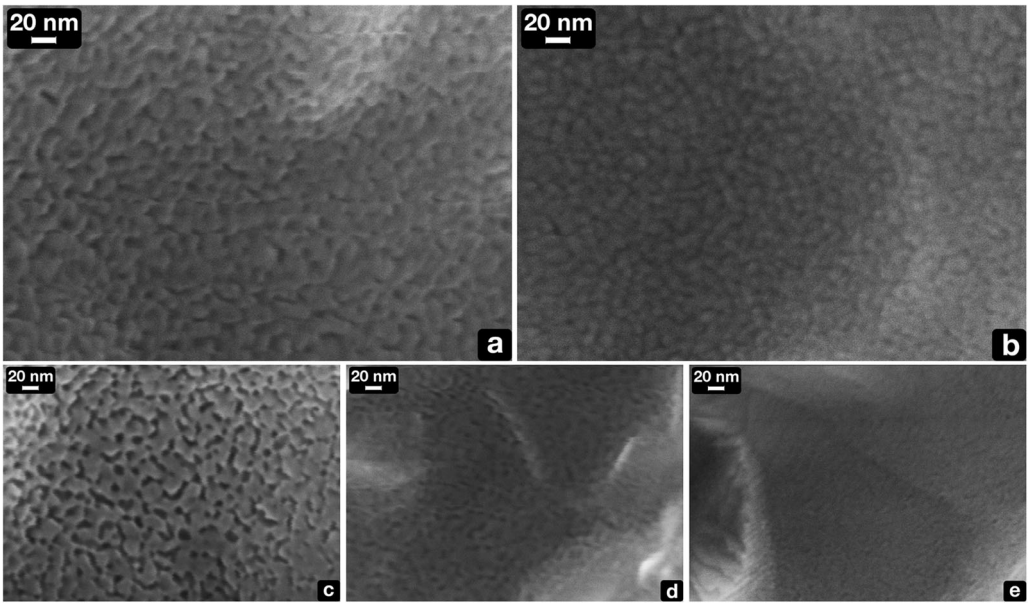

Fig. 4 SEM microphotographs for TiO_2–$xZrO_2$ ($x = 0$ **a**, 10 **b**, 20 **c**, 40 **d**, and 50 **e** mol.%) films

Table 1 Experimental and literature data for crystal lattice parameters of TiO_2–$xZrO_2$ ($x = 0$ and 10 mol.%) nanopowders and literature data for α-Al_2O_3 and $ZrTiO_4$ lattice parameters

Compound, phase	Lattice parameter, Å
TiO_2, anatase	$a = 3.7937(3)$, $c = 9.5219(1)$ $a = 3.7842$, $c = 9.5146$ [73]
$0.9TiO_2$–$0.1ZrO_2$, anatase	$a = 3.8041(6)$, $c = 9.6000(2)$
Substrate α-Al_2O_3, corundum	$a = 4.7644(1)$, $c = 13.0051(2)$ $a = 4.754$, $c = 12.99$ [74]
$ZrTiO_4$, zirconium titanate	$a = 4.808$, $b = 5.447$, $c = 5.032$ [70]

A film of TiO_2–$xZrO_2$ ($x = 50$ mol.%) composition, as well as the corresponding powder, is amorphous, most probably because of the low temperature of the xerogel treatment. Mean particle size, calculated from SEM data, is 7 ± 1 nm.

Morphology of a thin fim with TiO_2–$xZrO_2$ ($x = 10$ mol.%) composition was also investigated utilizing semi-contact AFM, including phase-contrast measurements. As can be observed from the obtained results presented in Fig. 5, on a flat surface area, a large number of small pores can be observed with size in the range of 12–17 nm and depth of about 5 nm, which correlates nicely with SEM data (Fig. 4b). Owing to the background noise and the resolution limitations from the probes (a resolution of only 6–10 nm can be achieved), it is hard to distinguish individual particles, however, some of them can be observed on the scan with phase contrast and have a size of about 10–12 nm.

Thus, it can be summarized that thin TiO_2–$xZrO_2$ ($x = 0$ and 10 mol.%) films possessing anatase structure were crystallized under relatively soft conditions (500 °C, 1 h, in air), and for the latter composition, particle size is much less (~30%) than that for pure titania.

3.3 Gas-sensing properties of TiO_2–$xZrO_2$ films

First of all, the sensitivity to oxygen of the obtained TiO_2–$xZrO_2$ ($x = 0$, 10, 20, 40, and 50 mol.%) thin-film nanomaterials was investigated. The selectivity to O_2 was tested in comparison with other analyte gases (CH_4, H_2, and CO). It was established that only semiconductor films with anatase structure (comprising ZrO_2 $0 \div 20$ mol.%) possess gas-sensing properties to chosen analytes at the operating temperatures of 400 and 450 °C.

A largely amorphous $ZrTiO_4$ film, containing 40 mol.% ZrO_2, under low temperatures, is a dielectric with a high dielectric constant [44, 48], and an amorphous TiO_2–$xZrO_2$ (with $x = 40$ mol.%) exhibited a high resistance of > 1 GΩ at the operating temperatures of ≤450 °C, so we were unable to measure their response.

As it is known, oxygen detection is possible due to the presence of oxygen vacancies ($V_o^{\bullet\bullet}$) in the anatase crystal structure [33, 34]. In an inert environment, equilibrium (3) will proceed according to a reverse reaction, yielding additional electrons and lowering the resistance. With the increase of oxygen concentration, equilibrium (3) will shift toward a direct reaction, causing the increase in resistance, which allows one to detect a response (R_{O2}/R_{Ar}).

$$1/2\,O_{2(g)} + 2e^- + V_o^{\bullet\bullet} \rightleftarrows O_o^x \quad (3)$$

TiO_2–$xZrO_2$ ($x = 0$ and 10 mol.%) films exhibited a high response to oxygen in a wide range of concentrations of

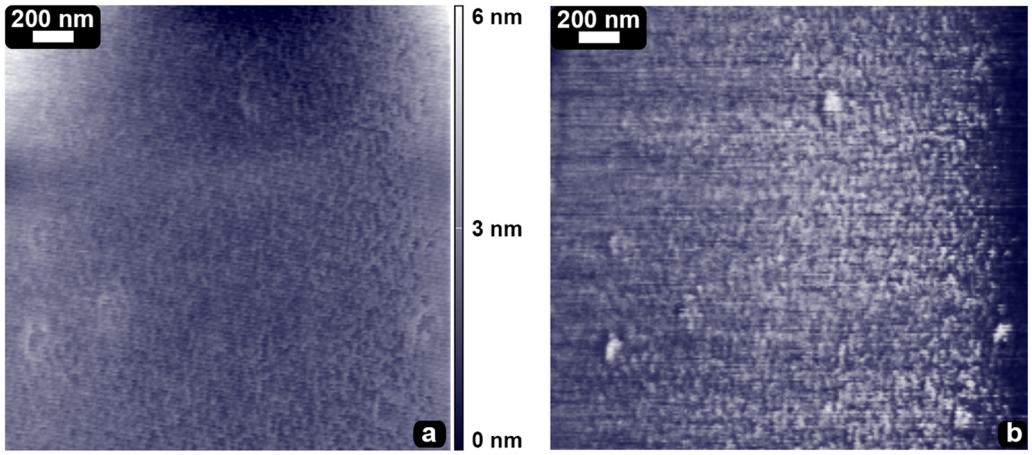

Fig. 5 AFM results for the TiO_2–$xZrO_2$ ($x = 10$ mol.%) film without **a** or with phase contrast **b**

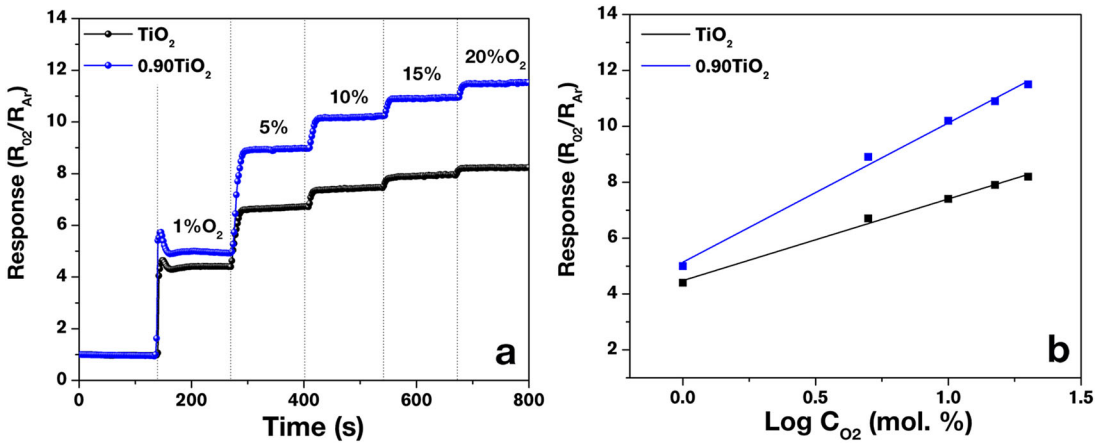

Fig. 6 Sensitivity of TiO_2–$xZrO_2$ ($x = 0$ and 10 mol.%) films at the operating temperature of 400 °C: experimental dependence of response (R_{O2}/R_{Ar}) from oxygen concentration **a** and the logarithmic dependence of response (R_{O2}/R_{Ar}) from oxygen content logarithm **b**

1–20% at the operating temperature of 400 °C (Fig. 6a). For pure TiO_2 with the increase of oxygen content from 1 to 20%, an increase in the response value (R_{O2}/R_{Ar}) from 4.4 to 8.2 is observed. Doping it with 10% ZrO_2 produces a significant increase of the response value (R_{O2}/R_{Ar}) from 5.0 to 11.5 for oxygen content from 1% to 20%, respectively. Such observations correlate well with the data obtained from SEM, according to which upon introduction of 10% ZrO_2, the solid solution is formed as a thin film with a lower particle size (9 ± 1 nm compared with 13 ± 2 nm for pure TiO_2). A more disperse state leads to a higher specific area of the receptor material, which promotes the surface processes and results in a higher response value (R_{O2}/R_{Ar}) compared with that of TiO_2.

Judging by literature data [75], doping of the anatase phase with 10% and 20% ZrO_2 results in changes in the electronic band structure with a widening of and a gap from 3.19 to 3.24 and 3.29 eV, respectively. In other words, an increase in the ZrO_2 content should result in a larger nanomaterial resistivity. In our case, the reverse is observed: as can be seen from Fig. 7, introduction of 10% ZrO_2 into the anatase structure facilitates the decrease in film resistivity both in the argon and the air atmosphere.

It should be noted that in this study, as well as in ref. [75], a decrease in the mean size of the film nanoparticles is observed from 13 to 9 nm. Therefore, it is difficult to differentiate between the effects of the dispersity factor and the chemical composition on the band gap value of semiconducting oxides.

In this work, we used an α-Al_2O_3 plate with a large roughness (R_a~400 nm) as a substrate for sensor materials. The features of sol–gel technology for obtaining oxide thin films include the steps of film deposition from precursor solution, its drying, and then crystallization during the heat treatment (after the hydrolysis and polycondensation processes have run their course), which induce a certain shrinkage. As a result of the large differences in height between Al_2O_3 substrate grains and the thermal expansion

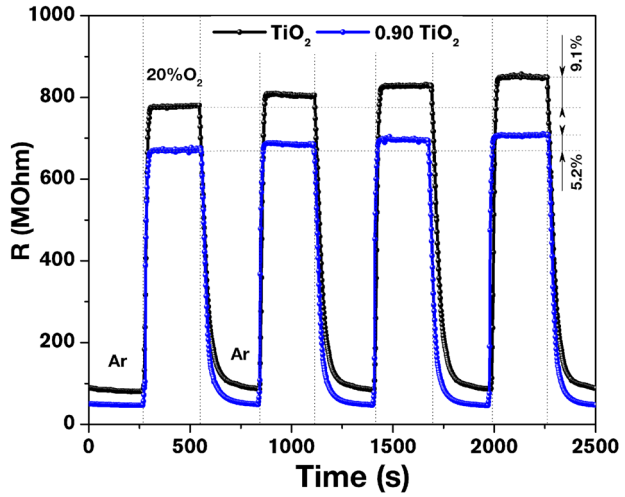

Fig. 7 Signal reproducibility on sensing 20% O_2 for TiO_2–$xZrO_2$ ($x = 0$ and 10 mol.%) films at the operating temperature of 400 °C

coefficients of the TiO_2–ZrO_2 nanomaterial and the substrate, fractures can occur in the films. In this study, the small mean size of the complex oxide nanoparticles might have allowed to obtain a more dense and continuous coating with a better contact between grains, which directly affects the sensor nanomaterial conductivity.

Thus, the conductivity of a thin-film semiconductor is dependent not only on its band gap width (which is affected both by its chemical composition and dispersity), but also on substrate characteristics and the approach utilized for its synthesis.

It seems that possibly besides the size factor, the increase in oxygen response under introduction of the Zr^{4+} cation into TiO_2 is also affected by an unavoidable increase in the number of defects in anatase structure, increase in oxygen atom mobility due to a larger length and a more ionic nature of the Zr–O bond, and also by the presence of a vacant 4d orbital in zirconium atoms, as shown in ref. [75]. However, in this study, the peculiarities of the electronic structure of synthesized TiO_2–$xZrO_2$ samples were not explored.

It should be noted that the response depends linearly on the logarithm of oxygen concentration (Fig. 6b), which is characteristic of defect semiconductor materials, such as TiO_2 or CeO_2 [33, 36], which are utilized to detect oxygen.

Reproducibility of TiO_2–$xZrO_2$ ($x = 0$ and 10 mol.%) films resistance upon detecting 20% O_2 is presented in Fig. 7. It is seen that after the injection of air (20% O_2), the baseline returns to the initial values. However, upon further oxygen injections, a drift in the resistance values is observed relatively to the first intake. After four repeating injections, the resistance values for pure TiO_2 increase by 9.1% and for the film doped by 10% ZrO_2 by 5.2%. This can be attributed to the occurrence of titanium +IV and +III formation reactions in the space between lattice points, which are possible under high temperatures (4)–(5) [76, 77]:

$$Ti_{Ti}^{x} + O_{o}^{x} \rightleftarrows Ti_{i}^{4\bullet} + 1/2O_2 + 4e^{-} \quad (4)$$

$$Ti_{Ti}^{x} + O_{o}^{x} \rightleftarrows Ti_{i}^{3\bullet} + 1/2\,O_2 + 3e^{-} \quad (5)$$

Reactions (4) and (5) are, as well as reaction (3), equilibrium reactions and proceed with the largest intensity in the inert environment. As can be seen from Fig. 7, return of the baseline resistance occurs reliably and with one and the same rate, in contrast to the values of resistance upon oxygen intake. These observations might lead to the conclusion that direct reactions (3)–(5) proceed with the same rate, while the corresponding reverse reactions proceed with differing rates, which could be due to the differing Ti^{3+} content in the crystal lattice after new intake of oxygen. Introduction of Zr^{4+} into the crystal lattice facilitates the substitution of titanium in its points, which unlike zirconium can switch from +IV state to +III. Thus, the stabilization of the lattice takes place, and for TiO_2–10% ZrO_2, composition reaction (4) occurs with lesser yield in the inert environment compared with TiO_2, which results in the decrease in the signal drift from 9.1 to 5.2% (Fig. 7).

Both for pure TiO_2 and TiO_2, doped with 10% ZrO_2, a slight decrease in the response value was observed when detecting more than 1% O_2 upon the increase of the operating temperature to 450 °C (Fig. 8). For the pure TiO_2 response, the increase in oxygen content from 1 to 20% changes from 3.7 to 6.4, and for the film with 10% ZrO_2—from 5 to 10.5. Thus, doping TiO_2 with zirconia leads to the diminishing decrease in the response value upon increasing the operating temperature of 400→450 °C. Diminishment is from 16% (TiO_2) to 0% (TiO_2–10 mol.% ZrO_2) when detecting 1% O_2 and from 22% (TiO_2) to 9% (TiO_2–10 mol.% ZrO_2) for detecting 20% O_2.

We were able to capture a small response at 450 °C for the TiO_2–$xZrO_2$ ($x = 20$ mol.%) film, which increased from 1.3 to 1.7 upon change of O_2 content from 1 to 20%. At the lower operating temperature (400 °C), the film resistance was higher than the measurement upper limit (>1 GΩ) due to the insufficient continuity of the film (Fig. 4c) and the presence of the amorphous particles, as is the case with the powder of the same composition (Fig. 1).

The time of response upon the change of oxygen content does not depend on the composition of the TiO_2–$xZrO_2$ ($x = 0$ and 10 mol.%) films. At the operating temperatures of 400 and 450 °C, response time upon the change of oxygen concentration from 0 to 1% was 6 s, with 12 more seconds required for complete stabilization of the signal. With the increase of the operating temperature from 400 to

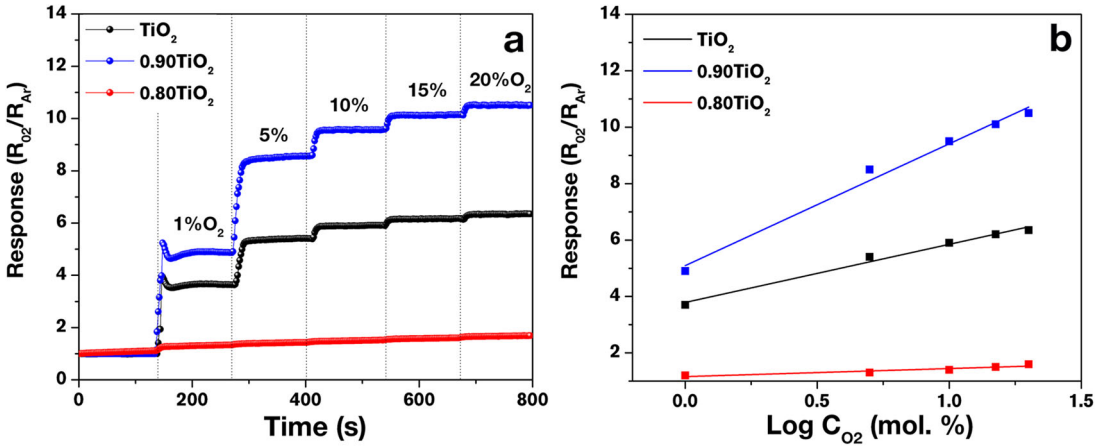

Fig. 8 Sensitivity to oxygen for TiO_2–$xZrO_2$ ($x = 0$, 10, and 20 mol.%) films at the operating temperature of 450 °C: experimental dependence of response (R_{O2}/R_{Ar}) from oxygen concentration **a** and the logarithmic dependence of response (R_{O2}/R_{Ar}) from oxygen content logarithm **b**

Table 2 Response time at the operating temperatures of 400 and 450 °C for TiO_2–$xZrO_2$ ($x = 0$ and 10 mol.%) films upon changing oxygen concentration

Change in oxygen content, "from-to", vol.%	Response time, s	
	400 °C	450 °C
0–1	6	6
1–5	19	17
5–10	13	10
10–15	10	9
15–20	8	7

450 °C, a small decrease in the response value occurs, as can be seen from Table 2. Upon oxygen concentration change from 1 to 5%, response time was 19 and 17 s, and for increase from 15 to 20%, response time equals 8 and 7 s — at 400 and 450°, respectively.

It should be noted that at 400 °C, the response time upon increase of oxygen content from 0 to 20% was 30 s, which proves the nonintegral character of response time changes upon the transition to higher oxygen concentrations. Such data are interesting from the point of evaluating the kinetic properties of the obtained receptor materials, which could be used in the sensors for oxygen detection in various application fields.

In order to evaluate the selective properties of the TiO_2–$xZrO_2$ ($x = 0$ and 10 mol.%) thin films, the responses to 0.2% H_2, CH_4, and 0.02% CO were also studied. As can be observed from the featured diagrams (Fig. 9), the films possess an excellent selectivity to oxygen, with responses (R_{air}/R_{gas}) to the mentioned analyte gases not exceeding 1.6 and 1.4 at the operating temperatures of 400 and 450 °C, respectively.

4 Conclusions

In this work, powders and thin films of TiO_2–$xZrO_2$ ($x = 0$, 10, 20, 40, and 50 mol.%) compositions were synthesized utilizing sol–gel technique with the use of metal alkoxoacetylacetonates as precursors. It was shown that the thin TiO_2–$xZrO_2$ ($x = 0$, 10, and 20 mol.%) films possess anatase crystal structure with mean particle sizes of 13, 8, and 28 nm, respectively, according to SEM, with the latter composition being significantly aggregated.

It was noted that due to the orienting effect of the α-Al_2O_3 substrate, the thin film with 40 mol.% ZrO_2 had signs of areas of regularity founded on srilankite $TiZrO_4$ (according to the Raman spectra). In the TiO_2–$xZrO_2$ ($x =$ 40 mol.%) powder, prepared by the similar technique, no such crystal nuclei were found.

TiO_2–$xZrO_2$ ($x = 0$ and 10 mol.%) films exhibited a high reproducible response to oxygen in a wide range of concentrations (1–20%) at relatively low operating temperatures of 400 and 450 °C. It was established that adding 10% ZrO_2 leads to the decrease in the mean particle size, which results in a higher response to oxygen in all the concentration ranges. A decrease in the response to oxygen upon increasing the operating temperature from 400 to 450 °C is also much less for the 10 mol.% ZrO_2 -doped titanium dioxide than for pure TiO_2. Introduction of the Zr^{4+} ion into the crystal lattice facilitates the decrease in baseline drift.

It was shown that the synthesized TiO_2–$xZrO_2$ ($x = 0$ and 10 mol.%) films possess a good selectivity to oxygen, with a response to other analyte gases (H_2, CH_4, and CO) not exceeding 1.6 and 1.4 at the operating temperatures of 400 and 450 °C, respectively.

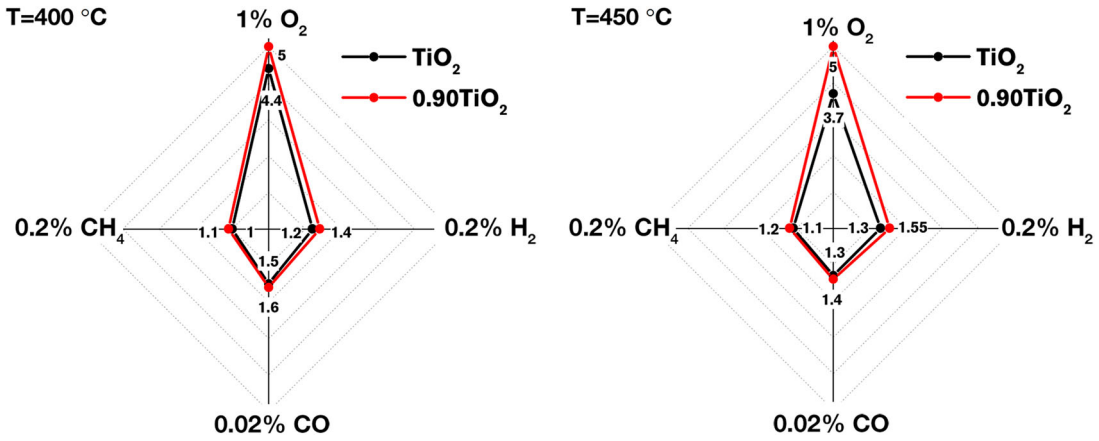

Fig. 9 Selectivity diagrams: dependence of TiO_2–$xZrO_2$ ($x = 0$, 10, and 20 mol.%) films response upon sensing 1% O_2 (R_{O2}/R_{Ar}), 0.2% H_2 and CH_4, and 0.02% CO (R_{air}/R_{gas}) at the operating temperatures of 400 and 450 °C

Synthesized precursors (zirconium–titanium acetylacetonates) can be utilized as functional inks for ink-jet printing for creation of receptive layers on multioxide sensors. Thus, the problem of miniaturization, concerning the production of MEMS that could detect various gases (including oxygen) utilizing numerous mathematical methods for signal processing, such as linear discriminant analysis (LDA) or principal component analysis (PCA), can be solved [78–80].

Acknowledgements This work was supported by IGIC RAS state assignment. The study has been funded by the Russian Foundation for Basic Research [project nos. 18-03-00992 (a study to the gas-sensing properties) and 18-33-20248 (development of precursors obtaining functional ink for ink-jet printing)].

Compliance with ethical standards

Conflict of interest The authors declare that they have no conflict of interest.

Publisher's note: Springer Nature remains neutral with regard to jurisdictional claims in published maps and institutional affiliations.

References

1. Chen X, Mao SS (2007) Titanium dioxide nanomaterials: Synthesis, properties, modifications and applications. Chem Rev 107:2891–2959. https://doi.org/10.1021/cr0500535
2. Anitha VC, Banerjee AN, Joo SW (2015) Recent developments in TiO_2 as n- and p-type transparent semiconductors: synthesis, modification, properties, and energy-related applications. J Mater Sci 50:7495–7536. https://doi.org/10.1007/s10853-015-9303-7
3. Hamilton JWJ, Entezari MH, Byrne JA et al. (2012) A review on the visible light active titanium dioxide photocatalysts for environmental applications. Appl Catal B Environ 125:331–349. https://doi.org/10.1016/j.apcatb.2012.05.036
4. Bavykin DV, Friedrich JM, Walsh FC (2006) Protonated titanates and TiO_2 nanostructured materials: Synthesis, properties, and applications. Adv Mater 18:2807–2824. https://doi.org/10.1002/adma.200502696
5. Magdysyuk OV, Adams F, Liermann HP, Spanopoulos I, Trikalitis PN, Hirscher M, Morris RE, Duncan MJ, McCormick LJ (2016) Understanding the adsorption mechanism of noble gases Kr and Xe in CPO-27-Ni, CPO-27-Mg, and ZIF-8. Int J Psychosoc Rehabil 20:1–6. https://doi.org/10.1039/c8tb00149a
6. Wang X, Zhao Y, Mølhave K, Sun H (2017) Engineering the surface/interface structures of titanium dioxide micro and nano architectures towards environmental and electrochemical applications. Nanomaterials 7:382. https://doi.org/10.3390/nano7110382
7. Tropis C, Rouhani MD, Landa G et al. (2011) A computational chemist approach to gas sensors: Modeling the response of SnO_2 to CO, O_2, and H_2O gases. J Comput Chem 33:247–258. https://doi.org/10.1002/jcc.21959
8. Thong LV, Hoa ND, Le DTT et al. (2010) On-chip fabrication of SnO_2-nanowire gas sensor: The effect of growth time on sensor performance. Sensors Actuators, B Chem 146:361–367. https://doi.org/10.1016/j.snb.2010.02.054
9. Lev O, Mokrushin AS, Medvedev AG et al. (2017) H_2O_2 induced formation of graded composition sodium-doped tin dioxide and template-free synthesis of yolk–shell SnO_2 particles and their sensing application. Dalt Trans 46:16171–16179. https://doi.org/10.1039/c7dt03104a
10. Hongsith N, Wongrat E, Kerdcharoen T, Choopun S (2010) Sensor response formula for sensor based on ZnO nanostructures. Sensors Actuators, B Chem 144:67–72. https://doi.org/10.1016/j.snb.2009.10.037
11. Kim W, Choi M, Yong K (2015) Generation of oxygen vacancies in ZnO nanorods/films and their effects on gas sensing properties. Sensors Actuators, B Chem 209:989–996. https://doi.org/10.1016/j.snb.2014.12.072
12. Kim HJ, Lee JH (2014) Highly sensitive and selective gas sensors using p-type oxide semiconductors: Overview. Sensors Actuators, B Chem 192:607–627. https://doi.org/10.1016/j.snb.2013.11.005
13. Persson P, Bergström R, Lunell S (2002) Quantum chemical study of photoinjection processes in dye-sensitized TiO_2 nanoparticles. J Phys Chem B 104:10348–10351. https://doi.org/10.1021/jp002550p
14. Samsudin EM, Abd Hamid SB (2017) Effect of band gap engineering in anionic-doped TiO_2 photocatalyst. Appl Surf Sci 391:326–336. https://doi.org/10.1016/j.apsusc.2016.07.007
15. Zhang M, Ning T, Zhang S et al. (2014) Response time and mechanism of Pd modified TiO_2 gas sensor. Mater Sci Semicond Process 17:149–154. https://doi.org/10.1016/j.mssp.2013.09.014
16. Neri G, Santangelo S, Donato N et al. (2011) Hydrogen sensing characteristics of Pt/TiO_2/MWCNTs composites. Int J Hydrogen

Energy 37:1842–1851. https://doi.org/10.1016/j.ijhydene.2011.10.017
17. Hazra SK, Tripathy SR, Alessandri I et al. (2006) Characterizations of porous titania thin films produced by electrochemical etching. Mater Sci Eng B Solid-State Mater Adv Technol 131:135–141. https://doi.org/10.1016/j.mseb.2006.04.004
18. Kim I-D, Lee S-J, Zyung T et al. (2010) Pd-doped TiO_2 nanofiber networks for gas sensor applications. Sensors Actuators B Chem 149:301–305. https://doi.org/10.1016/j.snb.2010.06.033
19. Muthukrishnan K, Vanaraja M, Boomadevi S et al. (2015) Highly selective acetaldehyde sensor using sol–gel dip coated nano crystalline TiO_2 thin film. J Mater Sci, Mater Electron 26:5135–5139. https://doi.org/10.1007/s10854-015-3041-0
20. Yin L, Zhang L, Lun N et al. (2010) Large scale synthesis and gas-sensing properties of anatase TiO_2 three-dimensional hierarchical nanostructures. Langmuir 26:12841–12848. https://doi.org/10.1021/la100910u
21. Hyun SK, Choi S, Sun G-J et al. (2017) Prominent gas sensing performance of TiO_2-core/NiO-shell nanorod sensors. J Nanosci Nanotechnol 17:4099–4102. https://doi.org/10.1166/jnn.2017.13409
22. Yang F, Zhu J, Zou X et al. (2018) Three-dimensional TiO_2/SiO_2 composite aerogel films via atomic layer deposition with enhanced H_2S gas sensing performance. Ceram Int 44:1078–1085. https://doi.org/10.1016/j.ceramint.2017.10.052
23. Ye Z, Tai H, Xie T et al. (2016) Room temperature formaldehyde sensor with enhanced performance based on reduced graphene oxide/titanium dioxide. Sensors Actuators, B Chem 223:149–156. https://doi.org/10.1016/j.snb.2015.09.102
24. Mor GK, Carvalho MA, Varghese OK et al. (2004) A room temperature TiO_2 nanotube hydrogen sensor able to self-clean photoactively from environmental contamination. J Mater Res 19:628–634
25. Liu L, Li X, Dutta PK, Wang J (2013) Room temperature impedance spectroscopy-based sensing of formaldehyde with porous TiO_2 under UV illumination. Sensors Actuators, B Chem 185:1–9. https://doi.org/10.1016/j.snb.2013.04.090
26. Chen CY, Chang KH, Chiang HY, Shih SJ (2014) Preparation of a porous ceria coating for a resistive oxygen sensor. Sensors Actuators, B Chem 204:31–41. https://doi.org/10.1016/j.snb.2014.07.053
27. Morante JR, Andreu T, Ghom SA et al. (2009) Oxygen sensing with mesoporous ceria–zirconia solid solutions. Sensors Actuators B Chem 140:216–221. https://doi.org/10.1016/j.snb.2009.02.078
28. Beie HJ, Gnörich A (1991) Oxygen gas sensors based on CeO_2 thick and thin films. Sensors Actuators B Chem 4:393–399. https://doi.org/10.1016/0925-4005(91)80141-6
29. Trinchi A, Li YX, Wlodarski W et al. (2003) Investigation of sol-gel prepared CeO_2-TiO_2 thin films for oxygen gas sensing. Sensors Actuators, B Chem 95:145–150. https://doi.org/10.1016/S0925-4005(03)00424-6
30. Liu Y, Zhou B, Cai W et al. (2008) Self-organized TiO_2 nanotube array sensor for the determination of chemical oxygen demand. Adv Mater 20:1044–1049. https://doi.org/10.1002/adma.200701619
31. Cabeza GF, Schipani F, Garetto TF et al. (2017) N-doping effects on the oxygen sensing of TiO_2 films. J Electroceramics 40:72–77. https://doi.org/10.1007/s10832-017-0100-3
32. Moseley PT (1992) Materials selection for semiconductor gas sensors. Sensors Actuators B Chem 6:149–156. https://doi.org/10.1016/0925-4005(92)80047-2
33. Ramamoorthy R, Dutta PK, Akbar SA (2003) Oxygen sensors: Materials, methods, designs. J Mater Sci 38:4271–4282. https://doi.org/10.1023/A:1026370729205
34. Wang H, Chen L, Wang J et al. (2014) A micro oxygen sensor based on a nano sol-gel TiO_2 thin film. Sensors (Switzerland) 14:16423–16433. https://doi.org/10.3390/s140916423
35. Park JY, Choi SW, Lee JW et al. (2009) Synthesis and gas sensing properties of TiO_2-ZnO core-shell nanofibers. J Am Ceram Soc 92:2551–2554. https://doi.org/10.1111/j.1551-2916.2009.03270.x
36. Mei Z, Xidong W, Fuming W, Wenchao L (2003) Oxygen sensitivity of nano-CeO_2 coating TiO_2 materials. Sensors Actuators, B Chem 92:167–170. https://doi.org/10.1016/S0925-4005(03)00259-4
37. Zhuiykov S, Wlodarski W, Li Y (2001) Nanocrystalline V_2O_5-TiO_2 thin-films for oxygen sensing prepared by sol-gel process. Sensors Actuators, B Chem 77:484–490. https://doi.org/10.1016/S0925-4005(01)00739-0
38. Dolgov L, Eltermann M, Lange S et al. (2017) Au/SiO_2 nanoparticles in TiO_2:Sm^{3+} films for improved fluorescence sensing of oxygen. J Mater Chem C 5:11958–11964. https://doi.org/10.1039/c7tc03704j
39. Mokrushin AS, Popov VS, Simonenko NP et al. (2017) Thin films of the composition 8% Y_2O_3–92% ZrO_2 (8YSZ) as gas-sensing materials for oxygen detection. Russ J Inorg Chem 62:695–701. https://doi.org/10.1134/s0036023617060213
40. Mohammadi MR, Fray DJ (2011) Synthesis and characterisation of nanosized TiO_2-ZrO_2 binary system prepared by an aqueous sol-gel process: Physical and sensing properties. Sensors Actuators, B Chem 155:568–576. https://doi.org/10.1016/j.snb.2011.01.009
41. Mortazavi Y, Elyassi B, Rajabbeigi N et al. (2005) Oxygen sensor with solid-state CeO_2–ZrO_2–TiO_2 reference. Sensors Actuators B Chem 108:341–345. https://doi.org/10.1016/j.snb.2004.12.079
42. Kashiwagi K, Shimizu K, Nishiyama H et al. (2007) Impedancemetric gas sensor based on Pt and WO_3 co-loaded TiO_2 and ZrO_2 as total NOx sensing materials. Sensors Actuators B Chem 130:707–712. https://doi.org/10.1016/j.snb.2007.10.032
43. Hsu CH, Tseng CF, Lai CH et al. (2010) Structural and electrical characteristics of ZrO_2-TiO_2 thin films by sol-gel method. Mater Sci Eng B Solid-State Mater Adv Technol 175:181–184. https://doi.org/10.1016/j.mseb.2010.07.010
44. Salahinejad E, Hadianfard MJ, MacDonald DD et al. (2013) Multilayer zirconium titanate thin films prepared by a sol-gel deposition method. Ceram Int 39:1271–1276. https://doi.org/10.1016/j.ceramint.2012.07.058
45. Anitha VS, Sujatha Lekshmy S, Joy K (2017) Effect of annealing on the structural, optical, electrical and photocatalytic activity of ZrO_2–TiO_2 nanocomposite thin films prepared by sol–gel dip coating technique. J Mater Sci, Mater Electron 28:10541–10554. https://doi.org/10.1007/s10854-017-6828-3
46. Park Y, Kim HG (1997) Electric-field-induced commensurate phase in $ZrTiO_4$. Appl Phys Lett 70:1971–1973. https://doi.org/10.1063/1.118795
47. Victor P, Krupanidhi SB (2005) Impact of microstructure on electrical characteristics of laser ablation grown $ZrTiO_4$ thin films on Si substrate. J Phys D: Appl Phys 38:41–50. https://doi.org/10.1088/0022-3727/38/1/009
48. Rouhani P, Salahinejad E, Kaul R et al. (2013) Nanostructured zirconium titanate fibers prepared by particulate sol-gel and cellulose templating techniques. J Alloys Compd 568:102–105. https://doi.org/10.1016/j.jallcom.2013.03.142
49. Gajović A, Šantić A, Djerdj I et al. (2009) Structure and electrical conductivity of porous zirconium titanate ceramics produced by mechanochemical treatment and sintering. J Alloys Compd 479:525–531. https://doi.org/10.1016/j.jallcom.2008.12.123
50. López-López E, Baudín C, Moreno R et al. (2012) Structural characterization of bulk $ZrTiO_4$ and its potential for thermal shock applications. J Eur Ceram Soc 32:299–306. https://doi.org/10.1016/j.jeurceramsoc.2011.08.004
51. Kim CH, Lee M (2002) Zirconium titanate thin film prepared by surface sol-gel process and effects of thickness on dielectric property. Bull Korean Chem Soc 23:741–744. https://doi.org/10.5012/bkcs.2002.23.5.741

52. Biju KP, Jain MK (2008) Sol-gel derived TiO_2:ZrO_2 multilayer thin films for humidity sensing application. Sensors Actuators, B Chem 128:407–413. https://doi.org/10.1016/j.snb.2007.06.029
53. Ansari ZA, Ko TG, Oh JH (2004) Humidity sensing behavior of thick films of strontium-doped lead-zirconium-titanate. Surf Coatings Technol 179:182–187. https://doi.org/10.1016/S0257-8972(03)00820-X
54. Sevastyanov VG, Simonenko EP, Simonenko NP et al. (2018) Sol-gel made titanium dioxide nanostructured thin films as gas-sensing materials for the detection of oxygen. Mendeleev Commun 28:164–166. https://doi.org/10.1016/j.mencom.2018.03.018
55. Castillero P, Roales J, Lopes-Costa T et al. (2017) Optical gas sensing of ammonia and amines based on protonated porphyrin/TiO_2 composite thin films. Sensors (Switzerland) 17:1–14. https://doi.org/10.3390/s17010024
56. Harrison CJ, Rashid SSAAH, Kandjani AE et al. (2018) Soot template TiO_2 fractals as a photoactive gas sensor for acetone detection. Sensors Actuators B Chem 275:215–222. https://doi.org/10.1016/j.snb.2018.08.059
57. Reddy YAK, Shin YB, Kang IK, Lee HC (2016) Substrate temperature dependent bolometric properties of TiO_{2-x} films for infrared image sensor applications. Ceram Int 42:17123–17127. https://doi.org/10.1016/j.ceramint.2016.07.225
58. Mokrushin AS, Simonenko EP, Simonenko NP et al. (2019) Oxygen detection using nanostructured TiO_2thin films obtained by the molecular layering method. Appl Surf Sci 463:197–202. https://doi.org/10.1016/j.apsusc.2018.08.208
59. Sao-Joao S, Viricelle JP, Kassem O et al. (2018) Synthesis and inkjet printing of sol–gel derived tin oxide ink for flexible gas sensing application. J Mater Sci 53:12750–12761. https://doi.org/10.1007/s10853-018-2577-9
60. Kemmitt T, Daglish M (2002) Decomposition of coordinated acetylacetonate in lead zirconate titanate (PZT) precursor solutions. Inorg Chem 37:2063–2065. https://doi.org/10.1021/ic971131c
61. Mokrushin AS, Simonenko EP, Simonenko NP et al. (2019) Gas-sensing properties of nanostructured $CeO_{2-x}ZrO_2$ thin films obtained by the sol-gel method. J Alloys Compd 773:1023–1032. https://doi.org/10.1016/j.jallcom.2018.09.274
62. Mokrushin AS, Simonenko EP, Simonenko NP et al. (2018) Tin acetylacetonate as a precursor for producing gas-sensing SnO_2 thin films. Russ J Inorg Chem 63:851–860. https://doi.org/10.1134/s0036023618070197
63. Maeder T, Simonenko NP, Vlasov IS et al. (2017) Synthesis of nanocrystalline ZnO by the thermal decomposition of [$Zn(H_2O)(O_2C_5H_7)_2$] in isoamyl alcohol. Russ J Inorg Chem 62:1415–1425. https://doi.org/10.1134/s0036023617110195
64. Le YK, Chen ZH, Bai LH et al. (2007) Phase transformation and particle growth in nanocrystalline anatase TiO_2 films analyzed by X-ray diffraction and Raman spectroscopy. Surf Sci 601:4390–4394. https://doi.org/10.1016/j.susc.2007.04.127
65. Manriquez ME, Picquart M, Bokhimi X et al (2008) X-ray diffraction, and Raman scattering study of nanostructured ZrO_2-TiO_2 oxides prepared by sol-gel. J Nanosci Nanotechnol 8:1–7. https://doi.org/10.1166/jnn.2008.041
66. Roy A, Sood AK (1995) Phonons and fractons in sol-gel alumina: Raman study. Pramana J Phys 44:201–209. https://doi.org/10.1007/BF02848471
67. Yin Z, Zhang WF, He YL et al. (2002) Raman scattering study on anatase TiO_2 nanocrystals. J Phys D: Appl Phys 33:912–916. https://doi.org/10.1088/0022-3727/33/8/305
68. Frank O, Zukalova M, Laskova B et al. (2012) Raman spectra of titanium dioxide (anatase, rutile) with identified oxygen isotopes (16, 17, 18). Phys Chem Chem Phys 14:14567–14572. https://doi.org/10.1039/c2cp42763j
69. Kim YK, Jang HM (2001) Lattice contraction and cation ordering of $ZrTiO_4$ in the normal-to-incommensurate phase transition. J Appl Phys 89:6349–6355. https://doi.org/10.1063/1.1368871
70. Do DB, Oanh LM, Van Minh N et al. (2016) Formation of crystal structure of zirconium titanate $ZrTiO_4$ powders prepared by sol–gel method. J Electron Mater 45:2553–2558. https://doi.org/10.1007/s11664-016-4412-x
71. Liu J, Li X, Zhao Q, Zhang D (2012) Influence of Structural and surface characteristics of $Ti_{1-x}Zr_xO_2$ nanoparticles on the photocatalytic degradation of methylcyclohexane in the gas phase María. Catal Sci Technol 2:1711–1718. https://doi.org/10.1039/c2cy20121f
72. Shannon RD, Prewitt CT (1968) Effective ionic radii in oxides and fluorides. Acta Crystallogr Sect B Struct Crystallogr Cryst Chem 25:925–946. https://doi.org/10.1107/s0567740869003220
73. Landmann M, Rauls E, Schmidt WG (2012) The electronic structure and optical response of rutile, anatase and brookite TiO2. J Phys Condens Matter 24. https://doi.org/10.1088/0953-8984/24/19/195503
74. Ishizawa N, Miyata T, Minato I et al. (1980) A Structural Investigation of α-Al2O3 at 2170 K. Acta Cryst B: 228–230. https://doi.org/10.1107/S0567740880002981
75. Mieritz DG, Renaud A, Seo DK (2016) Unusual changes in electronic band-edge energies of the nanostructured transparent n-type semiconductor Zr-doped anatase TiO_2 ($Ti_{1-x}Zr_xO_2$; x < 0.3). Inorg Chem 55:6574–6585. https://doi.org/10.1021/acs.inorgchem.6b00712
76. Li M, Chen Y (1996) An investigation of response time of TiO_2 thin-film oxygen sensors. Sensors Actuators, B Chem 32:83–85. https://doi.org/10.1016/0925-4005(96)80113-4
77. Lee DK, Jeon JI, Kim MH et al. (2005) Oxygen nonstoichiometry (δ) of $TiO_{2-\delta}$-revisited. J Solid State Chem 178:185–193. https://doi.org/10.1016/j.jssc.2004.07.034
78. Fedorov FS, Podgainov D, Varezhnikov A et al. (2017) The potentiodynamic bottom-up growth of the tin oxide nanostructured layer for gas-analytical multisensor array chips. Sensors (Switzerland) 17:2–12. https://doi.org/10.3390/s17081908
79. Nasibulin A, Sommer M, Plugin I et al. (2017) The Room-Temperature Chemiresistive Properties of Potassium Titanate Whiskers versus Organic Vapors. Nanomaterials 7:455. https://doi.org/10.3390/nano7120455
80. Fedorov F, Vasilkov M, Lashkov A et al. (2017) Toward new gas-analytical multisensor chips based on titanium oxide nanotube array. Sci Rep 7:1–9. https://doi.org/10.1038/s41598-017-10495-8